SCIENCE CHINA
Technological Sciences

•Article•

January 2024 Vol.67 No.1: 240–258
https://doi.org/10.1007/s11431-023-2510-x

Space advanced technology demonstration satellite

ZHANG XiaoFeng[1*], CHEN Wen[1], ZHU XiaoCheng[1], MENG Na[1], HE JunWang[1], BI XingZi[1], ZHANG YongHe[1*], SHI Qi[1], LI Fei[1], LIU Rui[1], FENG ZhengGong[1], LIU Liu[1], LI JinSong[1], WU HaiChen[1], XU DongXiao[1], LI TaiJie[1], HUANG JiangJiang[1], LIU Shuo[1], LI TianTong[1], YU XianSheng[1], GAO Yang[1], ZHOU Heng[1], BAN HanYu[1], ZHANG YanLi[1], ZHANG YueTing[1], YANG YingQuan[1], HE Tao[1], DUAN XuLiang[1], CHEN Xin[1], WANG YaMin[1], SUN AnTai[1], ZHANG KuoXiang[1], SUN Ying[1], WANG YaoBin[1], FAN ChengCheng[1], XIONG ShaoLin[2], LI XinQiao[2], WEN XiangYang[2], LING ZhiXing[3], SUN XiaoJin[4], ZHANG Chen[3], BAI XianYong[3], WANG ZhanShan[5], DENG YuanYong[3], TIAN Hui[6], YANG JianFeng[7], XUE HongBo[8], SANG Peng[8], LIU JinGuo[9], ZHENG HuiLong[10], ZHU Xiang[8], HE JianWu[11], LI Hui[12], XU LuXiang[13], XU ShuYan[14], CHEN WenWu[15], LIU ZhenDong[15], WANG ZhaoLi[16], MAO XiangLong[7], GAO Rong[7], LI ZongXuan[17], DING GuoPeng[1], WANG XinYu[1], DOU RunJiang[18], WENG LuBin[19], LUO Hao[20], WANG YaPing[1], LIANG XianFeng[8] & FANG ZiRuo[1]

[1] *Innovation Academy for Microsatellites, Chinese Academy of Sciences, Shanghai 201203, China;*
[2] *Institute of High Energy Physics, Chinese Academy of Sciences, Beijing 100049, China;*
[3] *National Astronomical Observatory of China, Beijing 100101, China;*
[4] *Shanghai Institute of Technical Physics, Chinese Academy of Sciences, Shanghai 200083, China;*
[5] *Institute of Precision Optical Engineering, School of Physics Science and Engineering, Tongji University, Shanghai 200092, China;*
[6] *School of Earth and Space Sciences, Peking University, Beijing 100871, China;*
[7] *Xi'an Institute of Optics and Precision Mechanics, Chinese Academy of Sciences, Xi'an 710119, China;*
[8] *National Space Science Center, Chinese Academy of Sciences, Beijing 100190, China;*
[9] *Shenyang Institute of Automation, Chinese Academy of Sciences, Shenyang 110016, China;*
[10] *Institute of Engineering Thermophysics, Chinese Academy of Sciences, Beijing 100190, China;*
[11] *Institute of Mechanics, Chinese Academy of Sciences, Beijing 100190, China;*
[12] *Shanghai Institute of Organic Chemistry, Chinese Academy of Sciences, Shanghai 200032, China;*
[13] *Hangzhou Institute for Advanced Study, University of Chinese Academy of Sciences, Hangzhou 310024, China;*
[14] *Nanyang Technological University, Singapore 569830, Singapore;*
[15] *Dalian Institute of Chemical Physics, Chinese Academy of Sciences, Dalian 116023, China;*
[16] *Technical Institute of Physics and Chemistry, Chinese Academy of Sciences, Beijing 100049, China;*
[17] *Changchun Institute of Optics, Fine Mechanics and Physics, Chinese Academy of Sciences, Changchun 130033, China;*
[18] *Institute of Semiconductors, Chinese Academy of Sciences, Beijing 100083, China;*
[19] *Institute of Automation, Chinese Academy of Sciences, Beijing 100190, China;*
[20] *School of Aeronautics and Astronautics, Zhejiang University, Hangzhou 310058, China*

Received April 30, 2023; accepted September 19, 2023; published online December 19, 2023

The Space Advanced Technology demonstration satellite (SATech-01), a mission for low-cost space science and new technology experiments, organized by Chinese Academy of Sciences (CAS), was successfully launched into a Sun-synchronous orbit at an

*Corresponding authors (email: zhangxf@microsate.com; zhangyh@microsate.com)

altitude of ~500 km on July 27, 2022, from the Jiuquan Satellite Launch Centre. Serving as an experimental platform for space science exploration and the demonstration of advanced common technologies in orbit, SATech-01 is equipped with 16 experimental payloads, including the solar upper transition region imager (SUTRI), the lobster eye imager for astronomy (LEIA), the high energy burst searcher (HEBS), and a High Precision Magnetic Field Measurement System based on a CPT Magnetometer (CPT). It also incorporates an imager with freeform optics, an integrated thermal imaging sensor, and a multi-functional integrated imager, etc. This paper provides an overview of SATech-01, including a technical description of the satellite and its scientific payloads, along with their on-orbit performance.

SATech-01, spacecraft design, scientific instruments, on-orbit performance

Citation: Zhang X F, Chen W, Zhu X C, et al. Space advanced technology demonstration satellite. Sci China Tech Sci, 2024, 67: 240–258, https://doi.org/10.1007/s11431-023-2510-x

1 Introduction

The Space Advanced Technology demonstration satellite (SATech-01), organized by the Chinese Academy of Sciences (CAS), serves as an experimental platform for the exploration of space science and the on-orbit demonstration of advanced common technologies. Developed by the Innovation Academy for Microsatellites, CAS (IAMC), the SATech-01 is equipped with 16 experimental payloads. These payloads incorporate diverse new materials, components, technologies, and instruments provided by over 20 institutes affiliated with CAS. SATech-01's test program encompasses 23 new technology verifications, which are all geared towards establishing a robust foundation for future space science exploration and application. In the lead up to its successful launch on July 27th, 2022, from the Jiuquan Satellite Launch Centre via the Lijian-1A (ZK-1A) rocket, SATech-01 underwent a flight design review (FDR) in June 2021, followed by a satellite flight acceptance review (FAR) in April 2022. The ZK-1A rocket, developed by CAS, is the first of its kind and the largest commercial solid rocket in China. SATech-01 is not only the primary satellite of ZK-1A but also the inaugural satellite of the Space Pioneer series. The diagrams of SATech-01 and ZK-1A are shown in Figure 1.

Post-launch, SATech-01 successfully executed the on-orbit testing of its platform. To date, the majority of the onboard payloads have undergone functional tests and performance verifications in orbit. Many significant scientific observation results have been obtained.

2 Mission overview

The most distinguishing feature of SATech-01 is its "multi-payload, multi-mode" approach. Unlike conventional satellites with payloads designed to serve a single dedicated objective, the SATech-01 satellite sets itself apart with its versatile nature. Equipped with 16 experimental payloads, it aims to achieve a wide range of verification targets spanning over various fields such as astrophysics, solar physics, earth observation, space environment monitoring, and more.

SATech-01, as depicted in Figure 2, is composed of both payloads and a platform. The payloads are categorized into four groups: Scientific instruments, remote-sensing cameras, propulsion systems, and new technology verification payloads, with the scientific instruments detailed in Section 3. The platform encompasses six subsystems: The Structures and Mechanisms Subsystem, the Thermal Control Subsystem, the Attitude and Orbit Control Subsystem, the Electrical Power Subsystem, the Communication Subsystem, and the On-Board Data Handling Subsystem. A more in-depth exploration of these subsystems can be found in Section 4.

SATech-01 operates on a 500 km Sun-synchronous circular orbit, boasting an orbital period of 94.75 min.

The diversity of payloads entails varying requirements for satellite design, particularly concerning its configuration and pointing mode. To cater to the diverse observational needs of different payloads, we have classified them into four categories:

(1) Payloads which require high-precision sun-pointing;
(2) Payloads which require earth-pointing;
(3) Payloads which require inertial-pointing;
(4) Payloads without specific pointing requirements.

To fulfill these mission observation requirements, the platform is designed to support various pointing modes, including high-precision sun-pointing ($-Z$ axis), earth-pointing ($+Z$ axis), and inertial pointing ($+X$ axis). Furthermore, SATech-01 also offers an offset sun-pointing mode specifically for the solar upper transition region imager's (SUTRI) calibration. The configuration of SATech-01, as shaped by the observational requirements of the payloads and the platform's pointing mode design, is illustrated in Figure 3. Table 1 provides a comprehensive list of SATech-01's main specifications.

The SATech-01 mission, designed and executed under the Chinese Academy of Sciences (CAS), comprises six systems: the satellite system, the launcher system, the launch site system, the TT&C (tracking, telemetry, and command)

Figure 1 Diagrams of SATech-01 and ZK-1A.

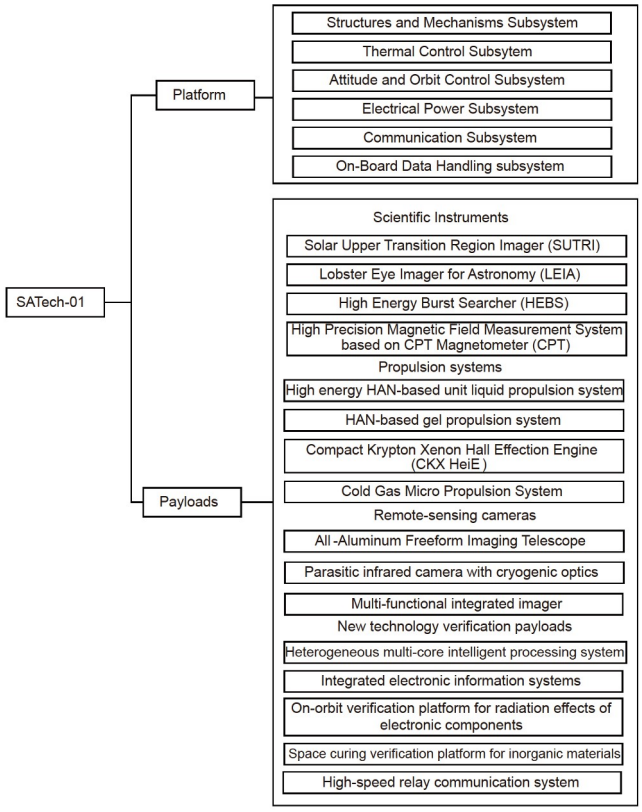

Figure 2 Product tree of SATech-01.

system, the ground support system, and the science application system.

(1) The SATech-01 satellite itself includes the platform and payload, with the payload further encompassing 16 distinct entities.

(2) The launcher system has been supplied by the Institute of Mechanics of CAS.

(3) The Jiuquan Satellite Launch Centre has provided the launch site system.

(4) The TT&C system is the contribution of Beijing Tianlian Measurement and Control Technology Co. LTD.

(5) The ground support system is facilitated by CAS, which also incorporates the use of the Beidou Short Message Service for real-time board-to-ground communication.

(6) The science application system is also provided by CAS.

The system architecture is illustrated in Figure 4.

Within just five days following the launch, the testing and commissioning phase of the satellite was largely completed. The results demonstrated that all operations, functions, and performance effectively met the stipulated requirements. Subsequently, payload experiments and calibrations were carried out in sequence: Starting with the scientific payloads, followed by imaging payloads, new technology payloads, and finally, propulsion payloads. This process spanned from August to November 2022. Upon completion of these steps, SATech-01 transitioned into its routine operational mode.

Given the considerations of power supply, data storage, and observation visibility, the payloads are designed to operate separately within solar illumination and earth eclipse regions. Data transmission tasks are given the highest priority, and they are not interfered by observational tasks. The earth-pointing observation task, managed by the science

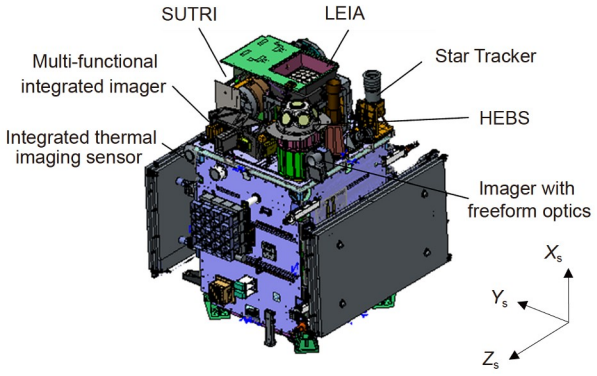

Figure 3 Diagram of SATech-01 configurations.

Table 1 Specifications of SATech-01

Parameter	Value
Weight	621.87 kg
Power consumption	717 W (Peak value)
Envelope	≤ϕ2250 mm×2076 mm (before launch) 5886 mm (*X*)×10578 mm (*Y*)×1422 mm (*Z*)
Bus voltage	(30±0.5) V
Absolute performance error	0.1°
Relative performance error	0.003°/s
Maneuver capability	90° in 10 min
Data transmission rate	≥450 Mbps
On-board storage	≥2 Tb
Orbit	500 km Sun-synchronous orbit
Lifetime	2 years

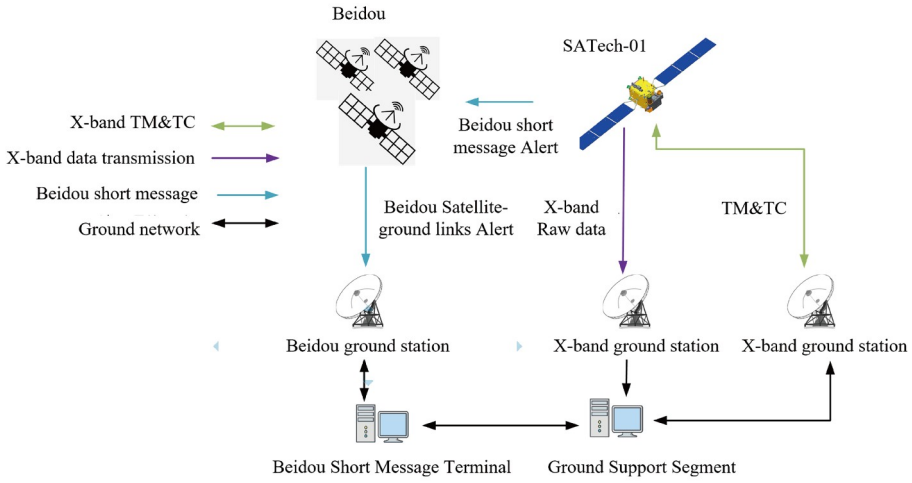

Figure 4 SATech-01 system architecture. TM&TC, Telemetry and Telecommand.

application system, is scheduled twice daily. When these tasks are not in process, SATech-01 switches to high-precision sun-pointing mode within the solar illumination region for SUTRI's operation, and to the inertial-pointing mode within the earth eclipse region for the lobster eye imager for astronomy's (LEIA) operation. Payloads such as high energy burst searcher (HEBS), CPT, and the on-orbit verification platform for radiation effects of electronic components are operational continuously. In transitioning between sun-pointing, earth-pointing, and inertial-pointing modes, the satellite can maneuver to its target pointing within less than 10 min.

3 Scientific instruments

SATech-01 is equipped with four primary scientific instruments: SUTRI, LEIA, HEBS, and CPT.

3.1 High energy burst searcher

HEBS is developed by the Institute of High Energy Physics, CAS (IHEP). Designed to monitor gamma-ray transients across the entire sky, with the energy range from 6 keV to 6 MeV, the HEBS is composed of two hemispherical domes. These domes follow the design of the gravitational wave high-energy electromagnetic counterpart all-sky monitor (GECAM) and are situated on the top and bottom of the SATech-01 satellite. Each dome is equipped with six gamma-ray detectors (GRDs) and one charged particle detector (CPD), as demonstrated in Figure 5.

For each dome, there are two types of GRDs: The detectors composed of LaBr3 crystals (LGRDs) and the detectors composed of NaI crystals (NGRDs). Both types of GRD are readout by SiPM array. There are two types of readout cases: The single channel and the dual channels (i.e., High-Gain and Low-Gain). All the basic information is listed in Table 2. The designed energy range for LGRD is 10–332 keV for High-Gain channel and 122–4500 keV for Low-Gain channel, and for NGRD the energy range is 10–355 keV for High-Gain channel and 122–5889 keV for Low-Gain channel. But for the NGRD with the single gain channel, its designed detection energy range is 10 to 700 keV [1].

3.2 Lobster eye imager for astronomy

LEIA is a fully representative test model of one of the 12 identical modules that comprise the Einstein Probe's wide-field X-ray telescope (EP-WXT), developed by the National Astronomical Observatories and the Shanghai Institute of Technical Physics, CAS. To demonstrate and optimize the

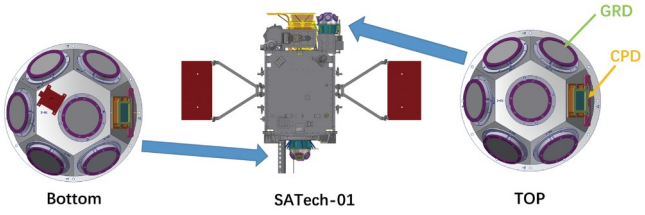

Figure 5 Installation position of HEBS and the installation location of detectors on HEBS.

Table 2 Specifications and performance of HEBS GRDs

Parameter	Value
Main detector	NaI (Tl); LaBr3 (Ce/Ce+Sr)
Detectors number	12
Energy range	15–4000 keV
Detection area	45.36 cm^2
Energy resolution in on-ground test	<18% @59.5 keV
Deadtime	4 μs
Detection efficiency at 15 keV	>75%

on-orbit performance of EP-WXT, a complete qualification module of WXT was launched into orbit on-board SATech-01, effectively serving as a pathfinder for the EP-WXT.

The EP-WXT module, comprised of an imaging system, electronics, thermal control, and mechanical structure, boasts main specifications outlined in Table 3. The imaging system itself consists of a mirror assembly (MA) and a focal detector array (refer to Figure 6, left). Harnessing the lobster-eye (LE) optics principle, the mirror is constructed from a 6×6 mosaic of micropore optics (MPO) plates, each shaped into a spherical curve with a 750 mm radius of curvature. The pores' reflective surfaces are coated with iridium. For more details on LEIA, refer to the description provided in refs. [2,3].

3.3 Solar upper transition region imager

SUTRI, which is developed by National Astronomical Observatories, CAS (NAOC), aims to test the on-orbit performance of the newly developed Sc/Si multi-layer reflecting mirror and the 2k×2k EUV CMOS imaging camera and to take full-disk solar images at the Ne VII 46.5 nm spectral line with a filter width of ~3 nm. SUTRI employs a Ritchey-Chr'etien optical system with an aperture of 18 cm, and more instrument characteristics are listed in Table 4.

With a unique filter centered at the Ne VII 46.5 nm line, SUTRI fills in the key temperature gap of current solar observations. Thus, SUTRI images will provide key information that is highly complementary to that obtained by other solar telescopes such as SDO/AIA and IRIS. SUTRI images have a field of view of ~41.6′×41.6′ and a mode rate spatial resolution of ~8″ without an image stabilization system. The normal cadence of SUTRI images is 30 s, and the solar observation time is about 16 h each day because the earth eclipse time accounts for about 1/3 of SATech-01's orbit period. The exploded diagram of SUTRI's optical and mechanical structure is shown in Figure 7 [4].

Table 3 Specifications and performance of LEIA[a)]

Parameter	Value
Number of MPO plates	36
Size of MPO plate (mm)	42.5×42.5×2.5
Size of pore (μm)	40×4
Focal length (mm)	376.8±1.1
Field of view	18.6°×18.6°
Angular resolution (arcmin)	3.8–7.5, ≤5 (85%)
Effective area* (cm^2)	2–3 @1 keV
Imaging sensors	4 CMOS sensors
CMOS dimensions (mm)	60×60
Pixel size (μm), number	15, 4k×4k
Bandpass (keV)	0.5–4.5
Energy resolution (eV)	130 @1.25 keV
Readout speed (ms)	50
Payload mass (kg)	26+27 (electronics)

a) The values were measured from the on-ground calibrations. * The effective area is for the central spot of the PSF.

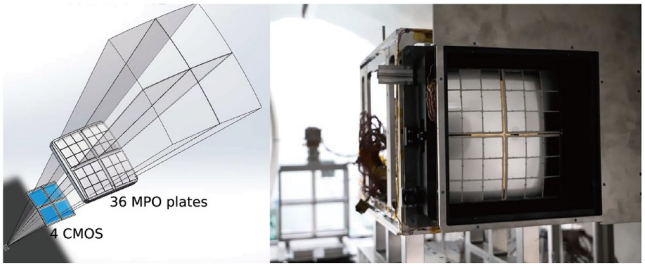

Figure 6 Left: Illustration of the configuration of the focusing mirror system, focal detector array, and FoV of LEIA. The mirror assembly is divided into four individual quadrants, each consisting of 3×3 MPO plates and associated with one of the four detectors. The overall FoV of the telescope module is 18.6°×18.6°. Right: A picture of the LEIA instrument undergoing on-ground X-ray calibration at IHEP before being assembled onto the SATech-01.

3.4 High precision magnetic field measurement system based on CPT magnetometer

The high precision magnetic field measurement system aimed to measure the global geomagnetic field, as shown in Figure 8, which is composed of a coherent population trapping magnetometer (CPTM), an anisotropic magneto resistance magnetometer (AMRM), a nano star tracker (NST), and a non-magnetic telescopic mast (TM). The CPTM is an optically pumped scalar magnetometer, which is based on two-photon spectroscopy of rubidium atoms and inherently enables omnidirectional, dead-zone-free measurements.

Table 4 Main instrument characteristics of SUTRI

Parameter	Value/Mode
Entrance aperture diameter	18 cm
Field of view	~41.6′×41.6′
Spatial resolution	~8″ (~1.22″/pixel)
Working line	Ne VII 46.5 nm
Formation temperature	0.5 MK
Filter width (FWHM)	~3 nm@46.5 nm
CMOS detector	2k×2k
Photon numbers (in theory)	Active Region: 700 photons/pixel/s Quiet Sun: 135 photons/pixel/s
Observing mode	Routine mode Dark calibration mode Flat field calibration mode Cleaning mode
Cadence	Routine mode: 30 s
Data rate	15 GB/day
Weight	~30 kg
Power	~30 W (without thermal control system)

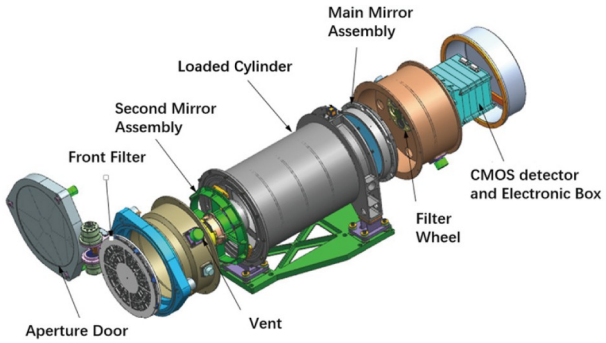

Figure 7 Exploded diagram of SUTRI's optical and mechanical structure.

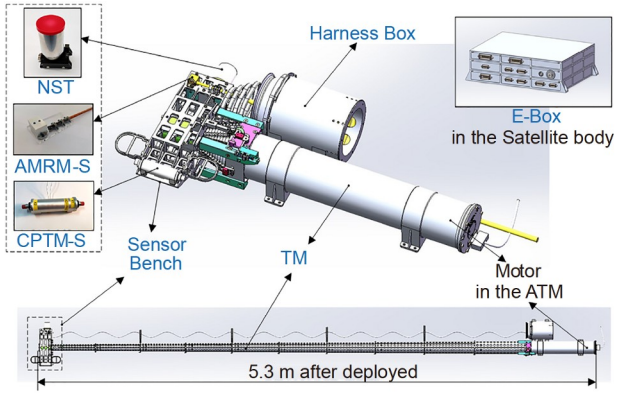

Figure 8 Diagram of the high precision magnetic field measurement system based on CPT magnetometer. CPTM-S: Sensor of the coherent population trapping magnetometer; AMRM-S: Sensor of the anisotropic magneto resistance magnetometer; NST: Nano star tracker; TM: Telescopic mast; E-Box: Electronics box.

This is the first domestic quantum/atomic magnetometer operating in space in China. Both the AMRM and NST are mounted on a stable bench attached to the TM. The NST is crucial for providing extremely accurate attitude measurements, which are necessary for the precise determination of the field vector as measured by the AMRM. The on-orbit implementation of the integrated detection technology for vector magnetic field and attitude has been successfully verified. The TM, deployed by an electric motor into a length of 5.3 m within approximately 20 min, carries the sensors on the bench away from the magnetic interference of the satellite platform. The National Space Science Center (NSSC), CAS, is responsible for this system and developed both the CPTM and AMRM. The NST and TM were developed by SatX Co. Ltd. and the Shenyang Institute of Automation (SIA), CAS, respectively. The ground performances of the payload are documented in Table 5. Additional details will be published in the future.

3.5 HAN-based gel propulsion system

The HAN (hydroxylamine nitrate)-based gel propulsion system is designed and manufactured by the Dalian Institute of Chemical Physics, CAS. This HAN-based gelled propellant avoids issues of storage, high toxicity, and environmental pollution typically associated with traditional liquid propellants. At the same time, it resolves the problems of poor thrust adjustability and reignition difficulty found in solid propellants. Compared with its counterparts, it is safer than liquid propellants and offers more flexible thrust control than solid propellants. The primary purpose of the HAN-based gel propulsion system is to verify the on-orbit performance of HAN-based gelled propellants. The system is situated at the satellite's bottom, as depicted in Figure 9. The primary features of the HAN-based gel propulsion system can be found in Table 6.

Table 5 Ground performances of the high precision magnetic field measurement system based on CPT magnetometer

Unit	Parameter	Value
CPTM	Measurement range	20000–80000 nT
	Linearity	0.0004%
	Sensitivity	≤0.01 nT/Hz$^{1/2}$@1 Hz
	Accuracy	0.3 nT (1σ)
	Sampling rate	40 Hz
	Power	<18 W
AMRM	Measurement range	±65000 nT
	Linearity	0.0006%
	Sensitivity	≤0.17 nT/Hz$^{1/2}$@1 Hz
	Data rate	20 Hz
	Power	<4 W
NST	Pointing accuracy	3.06″ (1σ)
	Rolling accuracy	27.09″ (1σ)
	Data rate	5 Hz
	Power	~0.85 W
TM	Deploy duration	20–25 min
	Fundamental frequency	1.76 Hz (Deployed)
	Length	950 mm (Stowed); 5300 mm (Deployed)
	Mass	14.45 kg

3.6 High energy HAN-based unit liquid propulsion system

High energy HAN-based unit liquid propulsion system is used for attitude and orbit control of micro satellites and synchronous orbit satellites. This propulsion system has four characteristics: (1) The density ratio of non-toxic unit propellants has been improved from generation to generation, reaching the international advanced level. (2) The structure and functionality of the system are highly integrated, with light weight and higher reliability. (3) The system is pre-

packaged, convenient to use, and has good universality. (4) A standardized 3U modular design is adopted, facilitating mass production. The high-energy HAN-based unit liquid propulsion system can be viewed in Figure 10. The main characteristics of this propulsion system are listed in Table 7.

3.7 Compact krypton xenon Hall effect ion engine

The compact krypton xenon Hall effect ion engine (CKX HeiE) is a collaborative effort by the Hangzhou Institute for Advanced Study, UCAS and Nanyang Technological University, Singapore. CKX HeiE adopts many new technologies, including krypton and xenon dual working fluid, multiple working modes, broadband thrust plasma propulsion technology; instant ignition technology; high-resolution micro Hall/cold air propulsion technology; intelligent pneumatic control and 3D printing high-pressure storage capacity; space environment and ionosphere analyser; multi-degree of freedom acceleration measurement, many of them are international pioneers [5]. CKX HeiE can be used as a power device for long-term, multi-maneuvering, and multi-mode deep space detectors, as well as for satellite attitude control, orbit maintenance, constellation formation configuration maintenance, and satellite departure, as shown in Figure 11. The main characteristics of compact krypton xenon Hall effect ion engine are listed in Table 8.

3.8 Cold gas micro propulsion system

Cold gas micro propulsion system is used to develop the

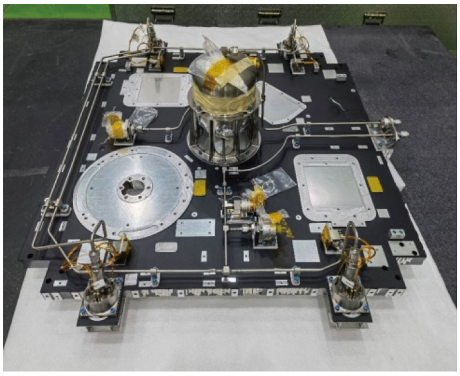

Figure 9 Picture of HAN-based gel propulsion system.

Table 6 Main characteristics of HAN-based gel propulsion system

Parameter	Value/Mode
Rated thrust	1 N (±10%)
Thrust misalignment	≤1°
Vacuum rated specific impulse	≥1960 N s/kg
Maximum stable working time	≥600 s
Cumulative pulse life times	≥50000
Number of warm start	≥300
Minimum time of pulse	30 ms

Figure 10 Picture of a high energy HAN-based unit liquid propulsion system.

Table 7 Main characteristics of high energy HAN-based unit liquid propulsion system

Parameter	Value/Mode
Propellant	High energy HAN-based HG-106
Thrust range	0.5–1.4 N
Thruster type	1 N
Rated steady-state specific impulse under operating conditions	230 s
System total impulse	1200 N s
Rated operating condition density specific impulse	310 s g cm^{-3}
System minimum impulse	≤0.1 N s
Warm start t_{80}	200 ms (@2.2 MPa), 600 ms (@0.8 MPa)
System dry weight	2.1 kg
Thruster preheating power	10 W
Propellant weight	0.9 kg
Warm start times	200 times

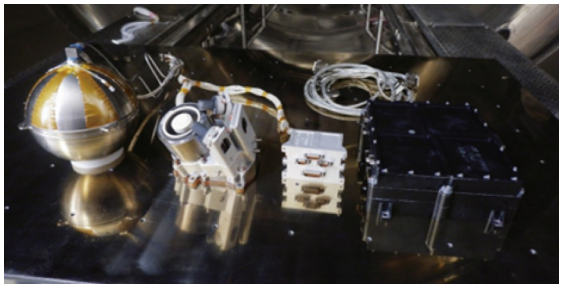

Figure 11 The picture of compact Krypton Xenon Hall effect ion engine.

Table 8 Main characteristics of compact Krypton Xenon Hall effect ion engine

Parameter	Value/Mode
Propellant	Xe, Kr
Thrust range	5–22 m N
Specific impulse	970–1700 s
Power dissipation	150–450 W
System dry weight	5.5 kg

space environment adaptability of the cold air micro thruster and the space fluid management performance of the plate type tank. The high-precision variable thrust cold air micro propulsion technology and the advanced plate type surface tension tank fluid management technology were conquered to meet the requirements of micro/nano satellite networking, low orbit satellite resistance compensation, attitude control and formation flying, and also applicable to the non-towing control task of space science satellites with ultra-high micro-*g* environment level, as shown in Figure 12. The main characteristics of the cold gas micro propulsion system are listed in Table 9.

3.9 Parasitic infrared camera with cryogenic optics

The parasitic infrared camera with cryogenic optics was designed by the Technical Institute of Physics and Chemistry, CAS. It is composed of an infrared detector, an optical system, and pulse tube cryocoolers (PTCs), as shown in Figure 13. The optical system adopts full transmission optics and integrates with the detector directly. The optical system and InSb infrared detector operate at 80–85 K to increase the detection sensitivity of the camera. The main characteristics are listed in Table 10.

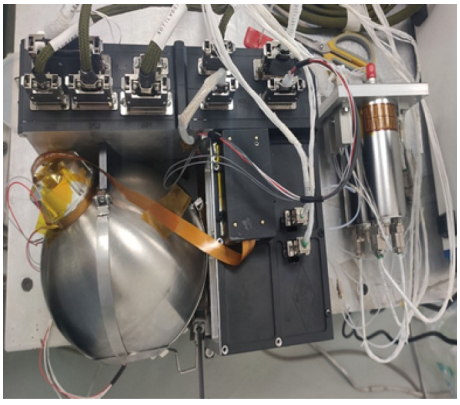

Figure 12 The picture of cold gas micro propulsion system.

Table 9 Main characteristics of cold gas micro propulsion system

Parameter	Value/Mode
Thrust range	PWM mode: 2–250 μN Proportion mode: 0.1–1000 μN Switch mode: 1 m N
Resolution ratio	PWM mode: 0.2 μN Proportion mode: 0.1 μN
Thrust noise	Proportion mode: 0.1 μN/Hz$^{1/2}$ (10 mHz–1 Hz)
Specific impulse	PWM mode/Proportion mode: >55 s (Thrust>10 μN) Switch mode: >45 s
Response time	PWM mode: <100 ms Proportion mode: <200 ms
Volume	1.5 L
Flow	0–100 sccm
Liquid center of mass shaking amplitude	Unidirectional acceleration of 10^{-2} m/s^2 not more than 20 mm
Liquid repositioning rate	50 mm/s
Discharge rate	98%
Power dissipation	<40 W
System weight	7 kg

3.10 All-aluminum freeform imaging telescope

The all-aluminum freeform imaging telescope (FIT) was designed by Xi'an Institute of Optics and Precision Mechanics, CAS. Compared with the traditional optical telescope, whose reflector is made of glass, both reflector and structure of all-aluminum FIT are made by the single-point diamond turning (SPDT) of aluminum alloy [6,7]. The all-aluminum FIT can achieve a large field of view, high resolution, light weight, and small volume at the same time. All-aluminum FIT contained three freeform mirrors (M1–M3), the support frame, two cover plates, and the external hood, as shown in Figure 14. Main instrument characteristics are listed in Table 11.

3.11 Multi-functional integrated imager

The multi-functional integrated imager, designed and developed by the Changchun Institute of Optics, Fine Me-

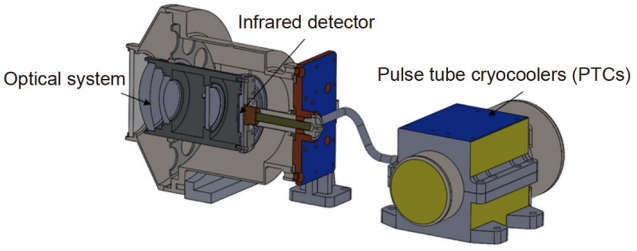

Figure 13 The diagram of the parasitic infrared camera with cryogenic optics.

Table 10 Main instrument characteristics of the parasitic infrared camera with cryogenic optics

Parameter	Value
Wavelength	3–5 μm
Field of view	10.7°×8.6°
Breadth	74 km×94 km@500 km
Resolution	147 m@500 km
Mass	15.1 kg
Power	103.1 W
Operating temperature (detector)	(80±0.3) K
Operating temperature (optical system)	85 K

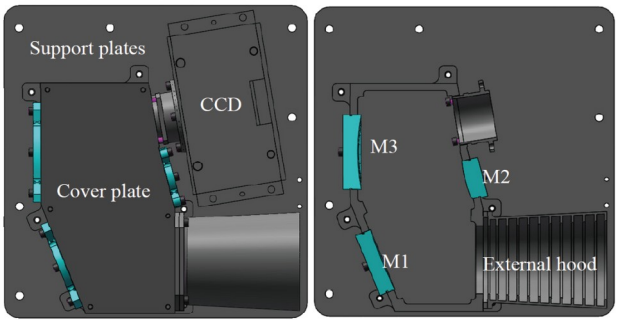

Figure 14 Three-dimensional model of all-aluminum FIT.

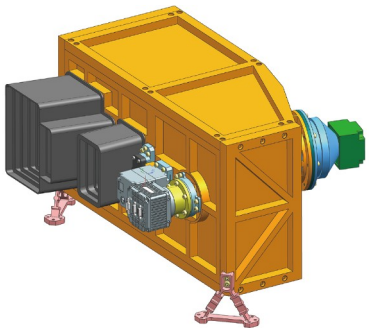

Figure 15 Diagram of multi-functional integrated imager.

Table 11 Main instrument characteristics of all-aluminum FIT

Parameter	Value
Wavelength	400–900 nm
Breadth	35 km×35 km@500 km
Resolution	17 m×17 m@500 km
Modulation transfer function	≥0.3@90 lp/mm (center of the FoV)
Mass	2.94 kg
Power	≤10 W
Operating temperature	−40°C–50°C

Table 12 Main instrument characteristics of multi-functional integrated imager

Parameter	Value/Mode
Wavelength	Visible light (450–800 nm) Low light (450–900 nm) Infrared (8–14 μm)
Working mode	Push broom/Staring
Resolution	5 m@500 km (Visible light) 20 m@500 km (Low light) 100 m@500 km (Infrared)
Breadth	28 km
Mass	17 kg
Power	60 W

chanics, and Physics, CAS, is a versatile imaging system that incorporates a visible camera, infrared camera, and low-light camera. This arrangement facilitates full-time space-based remote sensing of the Earth. The system can operate in both push broom and staring modes. During staring mode, the imager performs remote sensing imaging, while in push broom mode, it generates video imaging. A schematic of the multi-functional integrated imager can be seen in Figure 15, and the key characteristics of this instrument are detailed in Table 12.

3.12 Heterogeneous multi-core intelligent processing system

The heterogeneous multi-core intelligent processing system is the result of a collaborative effort by the IAMC, the Institute of Semiconductors, the Institute of Automation, CAS, and Zhejiang University. This system is equipped with three distinct artificial intelligence (AI) processing chips and relevant software. The primary objectives are to evaluate the long-term on-orbit performance of these processing chips and to ascertain the practicality of algorithms for remote sensing target detection and cell segmentation.

3.13 Integrated electronic information system

Designed by IAMC, the integrated electronic information system combines housekeeping, TT&C, and global navigation satellite system (GNSS) functionalities. This system, comprising integrated integronics and two antennas, is intended to confirm the system's feasibility and reliability for future satellite applications. Figure 16 presents an image of the system's integrated integronics, while Table 13 provides a list of its primary characteristics.

3.14 On-orbit verification platform for radiation effects of electronic components

The on-orbit verification platform for radiation effects of electronic components employs an inclusive testing technology for multi-device performance and key functions [8,9]. Designed modularly, it enables real-time, comprehensive monitoring of functional performance for numerous types and quantities of crucial large-scale integrated circuit devices on satellites. It assesses components' resistance to radiation effects like the single particle and the total dose in orbit, and it can analyze potential radiation effects in terms of location, propagation mechanism, and manifestation. Furthermore, it supports plug-and-play functionality and swift verification of space components, meeting the flight application testing demands of aerospace devices, as shown in Figure 17. Table 14 lists the platform's primary characteristics.

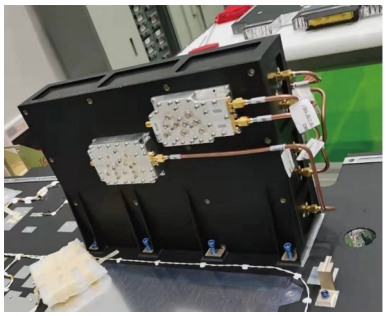

Figure 16 Image of integrated integronics of integrated electronic information system.

Table 13 Main characteristics of integrated electronic information system

Parameter	Value
CPU	48 MHz
PROM	2 MB
SRAM	8 MB
Mass (integronics)	1.2 kg
Power	28.2 W (Peak)

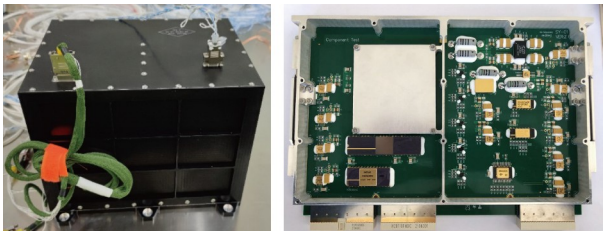

Figure 17 The picture of on-orbit verification platform for radiation effects of electronic components.

Table 14 Main characteristics of on-orbit verification platform for radiation effects of electronic components

Parameter	Value/Mode
Voltage measurement accuracy	≤0.04 mV
Current measurement accuracy	≤0.01 mA
Reading and writing frequency	≥100 MHz
Electrical parameter testing cycle	≤0.1 s
Data/functional testing cycle	≤1 s

3.15 Space curing verification platform for inorganic materials

The space curing verification platform for inorganic materials is to verify the curing performance of fibre reinforced inorganic composites based on the ground folding, space deployable irreversible curing in the space environment can continuously heat the inorganic materials at a constant temperature, continuously monitor and collect the surface image information of the entire test process of inorganic materials, evaluate the internal curing state, and deeply study the impact of space Micro-*g* environment on the flow, reaction, curing and other processes of inorganic micro powder. Provide technical reserves for the construction of large inflatable deployable flexible spacecraft in the future, as shown in Figure 18. The main characteristics of space curing verification platform for inorganic materials are listed in Table 15.

3.16 High-speed relay communication system

The high-speed relay communication system, conceived by the National Space Science Center, CAS, is dedicated to validating the satellite's relay communication function and performance between space and ground. The system comprises an L-band phased array front end, a power divider, a signal processing unit, and a modulator circuit, capable of achieving a data rate of up to 8 Mbps. Figure 19 presents a diagram of the high-speed relay communication system, and its primary characteristics are detailed in Table 16.

4 Satellite design

4.1 Structures and mechanisms subsystem

The SATech-01 employs a frame-panel structural design. As depicted in Figure 20, the core support frame comprises the bottom frame, vertical bar, rocket-attached joint, and the

Figure 18 Picture of space curing verification platform for inorganic materials.

Table 15 Main characteristics of space curing verification platform for inorganic materials

Parameter	Value/Mode
Pressure	≥200 N
Pressure stroke	≥10 mm
Monitor camera frame rate	≥10 fps
Monitor camera resolution cycle	≥1 Mpixel
Data/functional testing cycle	≤1 s

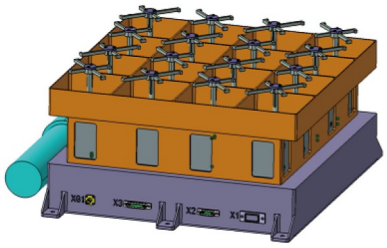

Figure 19 Diagram of high-speed relay communication system.

Table 16 Main characteristics of high-speed relay communication system

Parameter	Value/Mode
Frequency stability	Better than $\pm10^{-6}$/day
Bit rate	8 Mbps (QPSK modulation)
Phase noise	≤−50 dBc (10 Hz)
	≤−60 dBc (100 Hz)
	≤−70 dBc (1 kHz)
	≤−80 dBc (10 kHz)
	≤−90 dBc (100 kHz)
	≤−110 dBc (1 MHz)
Mass	12.87 kg
Power	60 W

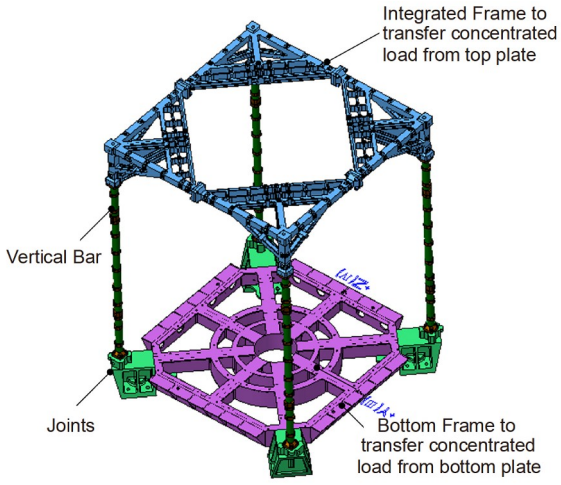

Figure 20 The main support frame of the SATech-01.

integrated frame positioned at the satellite's apex. This main frame is rigidly interconnected with six panels to create a comprehensive enclosure. The main supporting frame seals the box, reinforcing its load-bearing capacity. Together, the support frame and box form the primary load-bearing structure of the satellite, bearing and distributing the longitudinal, lateral, and torsional loads of the entire spacecraft, as illustrated in Figure 21.

The satellite utilizes a primarily rectangular frame-panel design, comprising the frame, pole, and six lateral plates which serve as the primary installation sites for equipment. To ensure expedient payload replacement and maintenance during the development phase, an open payload module design is incorporated into the top panel. The satellite derives its energy from symmetrically folded solar arrays. These solar arrays, located on the $\pm Y$ sides of the satellite during launch, unfurl along the $\pm Y$ axis once in orbit, as depicted in Figure 22.

The SATech-01 and ZK-1A rocket are connected using 4-point explosive bolts, with the connecting point forming a circle with a diameter of φ1090 mm. During the separation of the satellite and the rocket, a spring push rod mechanism is employed.

4.2 Thermal control subsystem

To accommodate the characteristics of orbit and attitude, the SATech-01 satellite incorporated cooling coatings on its four lateral panels. Specifically, the $-X$ panel, which directly faces the Sun, employed an OSR coating. Heat dissipation was achieved by installing thermal equipment on the lateral panels. The base panel equipment relied on thermal radiation through the lateral panels for dissipation. Active thermal control, insulation installation, and MLI (multi-layer in-

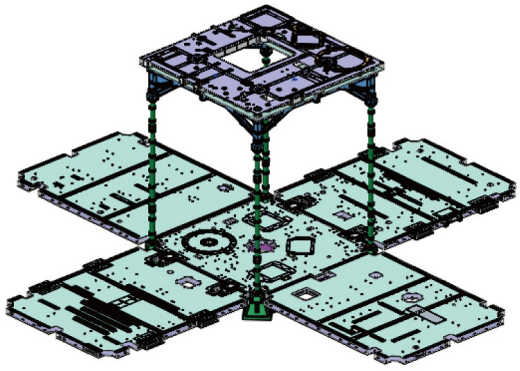

Figure 21 Exploded diagram of SATech-01's mechanical structure.

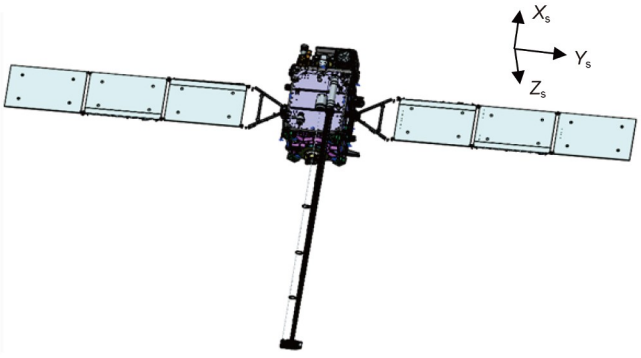

Figure 22 Diagram of SATech-01 (deployed).

sulation) coating were implemented for components such as the battery, star trackers, and main propulsion system. Within the satellite platform, high infrared emissivity coating and heat pipes were utilized to enhance thermal equilibrium among the equipment.

Based on the functional characteristics of the payloads and their specific temperature requirements, a spacecraft-level thermal design was conducted. An important aspect of this design was the careful arrangement of the payloads, considering their optimal layout. Table 17 illustrates that the majority of the optical payloads were centrally positioned on the top panel of the platform. By implementing a decoupling design and zoned temperature control for the top panel, the thermo-elasticity and temperature gradient properties were minimized. The electronic equipment of the payloads was uniformly installed on the lateral panels and co-designed with the platform's equipment to facilitate heat dissipation. This thermal layout approach improved the adaptability and coordination between the payloads and the platform while also saving significant development time and cost.

For the thermal design of the payloads, precise temperature control was implemented for various optical modules, including SUTRI, LEIA, the integrated thermal imaging sensor, and the multi-functional integrated imager. The heat generated by the detectors was efficiently conducted to radiators using heat pipes or conduction structures. HEBS (high-energy beam-splitters) employed a decoupling method to achieve high-precision temperature control at lower temperature levels. Figure 23(a) provides an illustration of the final thermal status of the payloads on the $-Z$ side.

An adaptive deployable radiator system was designed for the high-power communication payload, as depicted in Figure 23(b). This system was specifically developed to effectively dissipate heat generated by the payload, up to 200 W, within a 25-min timeframe. It incorporated adaptive thermal adjustment mechanisms to accommodate the payload's actual working conditions [10].

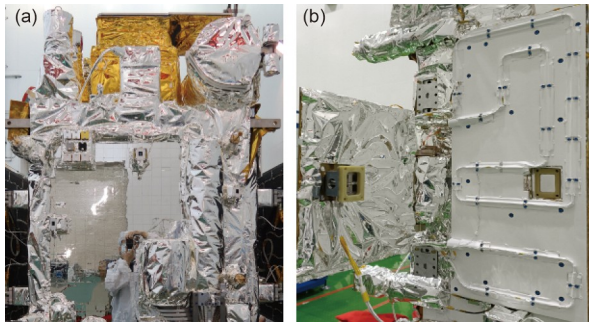

Figure 23 (a) Final thermal status of the $-Z$ side payloads; (b) deployable and adaptive intelligent thermal control system.

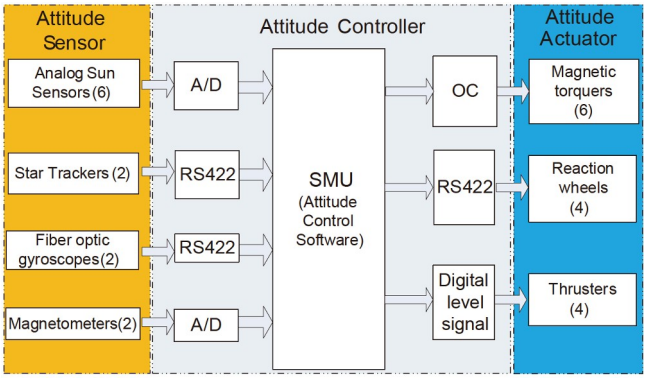

Figure 24 Block diagram of attitude and orbit control system.

4.3 Attitude and orbit control subsystem

The block diagram of the attitude and orbit control system (AOCS) is presented in Figure 24. To enhance the efficiency of a single star sensor during the load task, two star trackers are employed as hot backups. By fusing the data from both star trackers and applying EKF (extended Kalman filter) filtering with the gyro component data, the system achieves high-precision attitude determination, meeting the required performance standards. The angular velocity of the satellite is measured with exceptional precision using two three-axis integrated fiber optic gyro components, ensuring the satellite maintains the desired level of stability.

The three-axis magnetometers and analog sun sensors are employed as well-established components in the system. The magnetometers utilize a hot standby mode with two probes to enable all-weather measurement of the geomagnetic vector. Analog sun sensors are utilized to provide a near-all-sky spherical field of view and measure the solar vector. The

Table 17 Payload thermal layout design

Payload	Location/Function	Mounting	Independent temperature control
SUTRI, LEIA, HEBS, Multi-functional integrated imager	Top panel (Detection)	Insulation	Yes
CPT HAN-based propulsion	$-Z$ panel (Mechanism/Propulsion)	Insulation	
High power unit and deployable radiator system	$-Y$ panel (Equipment/Mechanism)	Insulation	
Integrated thermal imaging sensor	$+Y$ panel (Detection)	Insulation	
CKX HeiE	Base panel (Propulsion)	Insulation	
Cold gas micro propulsion system	$+Z$ panel (Propulsion)	Insulation	
Electronic equipment	Lateral panels	Conduction	No

combination of three-axis magnetometers and analog sun sensors allows for rough attitude determination, meeting the requirements of on-orbit acquisition and safe mode attitude determination.

In Figure 24, the attitude and orbit control system includes four reaction wheels as the primary actuator, arranged in a three-positive and one-angle configuration. These reaction wheels are responsible for absorbing angular momentum during the on-orbit phase, thereby meeting the requirements of mitigating space interference torque and performing attitude maneuvers in orbit. Additionally, six magnetic torquers are utilized to unload momentum from the reaction wheels and provide control during the on-orbit phase and safety mode operations. Thrusters are employed for debris avoidance and deorbit maneuvers.

4.4 Electrical power subsystem

The electrical power system of the SATech-01 satellite comprises three main components: The solar array, lithium battery pack, and power controller. This subsystem is responsible for managing the generation, storage, and distribution of electrical power required by the spacecraft. The satellite is equipped with a solar panel that covers an area of approximately 4.5 m^2. For power storage, a high-performance lithium battery pack with a total capacity of 101 A h is selected. The power system follows a regulated bus architecture based on the sequential switching shunt series regulator (S4R). This architecture ensures a nominal bus voltage of (30±0.5) V. During the end of the satellite's lifetime, the power system can provide a power supply capacity exceeding 1200 W.

4.5 Communication subsystem

The communication subsystem of the SATech-01 satellite comprises three main modules: the TT&C module, the Beidou short message module, and the data transmission module.

The TT&C module utilizes a spread spectrum system to complete traditional satellite telemetry and telecommand processing. The Beidou short message module utilizes the Beidou short message function to transmit important observation information of on-board payloads to the ground in near real-time. The data transmission module stores on-board payload data and satellite engineering data, and communicates with the ground at high speed through a phased array.

The main technical indicators of each module are shown in Table 18.

Table 18 Specifications of communication subsystem

Modules	Parameter	Value
TT&C	System design	Bi-directional incoherent spread spectrum communication
	Frequency band	X-band
	Telecommand data rate	4000 bps
	Telemetry data rate	16384 bps
Beidou short message	Modulation	Spread spectrum communication
	Frequency band	L-band
	Data rate	400 bps
Data transmission	Modulation	QPSK
	Frequency band	X-band
	Data rate	450 Mbps
	Sweep range	Rotation angle: ±360°; off-axis angle: ±67°

4.6 On-board data handling subsystem

The On-board data handling subsystem of the SATech-01 satellite consists of two main components: The satellite management unit (SMU) and the GNSS. The SMU is responsible for controlling and commanding the activities of platform units and payloads. It performs various functions such as flight dynamics control, AOCS data processing, telemetry control, and power and thermal control, among others. The avionic architecture of SATech-01 is depicted in Figure 25. The instrument control unit (ICU) collects various types of information, which is then transmitted to the SMU through different interfaces such as CAN (controller area network), asynchronous serial port, and synchronous serial port. Table 19 provides the total number of channels for the different interfaces used in the data transmission and communication within the satellite system.

5 Satellite environment tests

To ensure the reliability and readiness of the satellite's mechanical and thermal design, as well as the electrical interface of satellite equipment, a comprehensive set of functional and performance tests, along with environment acceptance tests, are conducted.

5.1 Mechanical test

To validate the satellite design, sinusoidal vibration and sound experiments were conducted. The purpose of these tests was to: (1) Verify the rationality of the satellite's structural design and the effectiveness of the manufacturing process. (2) Test the satellite's ability to withstand vibrations and sound levels at the acceptance criteria. (3) Assess the normal functionality of the solar array's expansion mechanism after being exposed to the acceptance level vibration

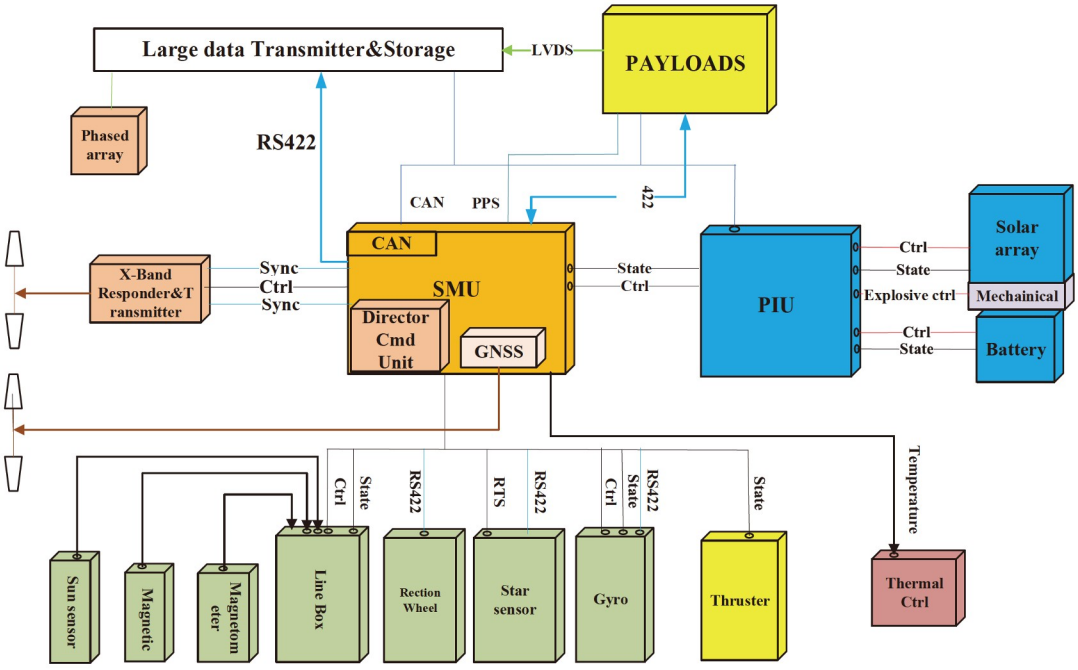

Figure 25 Avionics architecture of SATech-01.

and sound environment. (4) Verify the proper operation of the CPT's extender mechanism following the acceptance level vibration and sound environment. (5) Confirm the normal expansion function of the deployable radiator after being subjected to the acceptance level vibration and sound environment.

The SATech-01 satellite successfully passed the sinusoidal vibration and sound environments test at the acceptance level without encountering any issues of being undertested or overtested (Figure 26).

The analysis of the sound environment results suggests that the actual random vibration response of the satellite's payload, individual components, and solar array is reasonable. Furthermore, the random vibration conditions experienced by each individual component are within reasonable parameters.

Table 19 Communication interfaces of SATech-01

Communication Interface	Channel
Analog digital	101+225
Open Collector (OC) output	91
Open Collector (OC) input	4
Universal asynchronous receiver/transmitter (UART-422)	30
Synchronous serial interface (SSI)	4
Pulse per second (PPS) input	2
Controller area network (CAN) channel	2

5.2 Electro magnetic compatibility (EMC) test

The electro magnetic compatibility (EMC) test is conducted to assess the EMC between the platform's subsystems and integrated payloads within the flight module of SATech-01 (Figure 27). The primary objective is to validate the effectiveness of the satellite's electromagnetic compatibility design and identify any potential hidden risks or defects. The test consists of several stages, including environmental inspection, signal calibration, compatibility testing under different operational modes, and electromagnetic environment

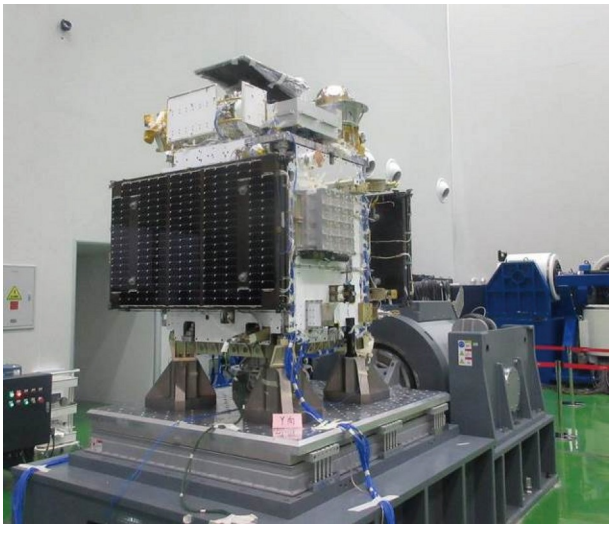

Figure 26 *Y*-axis vibration experiment of SATech-01.

monitoring. The test results indicate that the platform's devices and integrated payloads perform well across various working modes, demonstrating good compatibility.

5.3 Thermal test

The thermal balance test at the spacecraft level primarily assesses the performance of the thermal control subsystem in maintaining the equipment within specified temperature ranges. The thermal vacuum cycling test is conducted to detect potential early failures caused by quality defects in components, materials, processes, and manufacturing.

As depicted in Figure 28, SATech-01 satellite utilized an infrared lamp array to simulate heat flux within the vacuum chamber during the thermal tests. Following these tests, it was observed that the equipment temperatures remained within a reasonable range. This indicates that the thermal design of the satellite is deemed reasonable, with good product and equipment performance, and is a normal thermal control status.

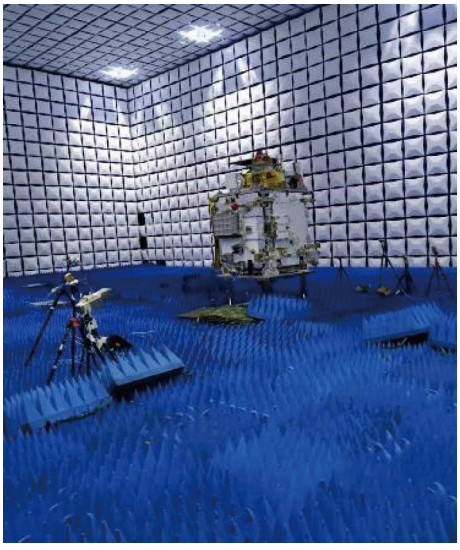

Figure 27 EMC test of SATech-01.

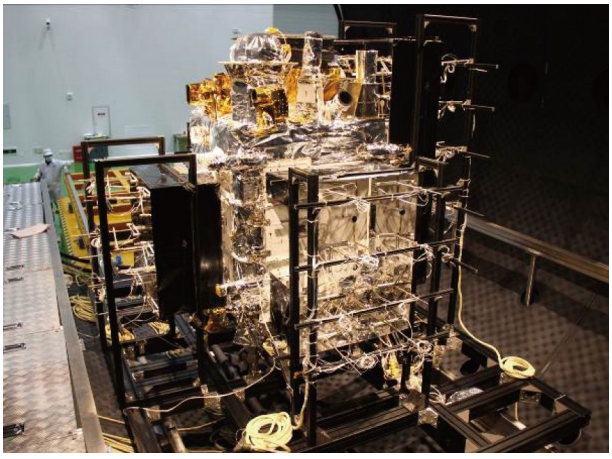

Figure 28 Thermal test of SATech-01.

5.4 Magnetic test

To understand the magnetic characteristics of SATech-01 and ensure that the remanence of each axis remains below 1 A m^2 in all working modes, a magnetic test was conducted. The magnetic flux method was employed to measure the remanence of the satellite, as illustrated in Figure 29. Following the initial measurements, magnetic compensation was performed due to excessive remanence observed in the *X*-axis. Subsequent magnetic testing, after the compensation, demonstrated that the remanence of each axis met the required specifications. Additionally, the change in the module value of the magnetometer caused by the magnetic compensation was found to be within 1000 nT.

6 On-orbit performance

6.1 Platform

After the successful launch, the SATech-01 satellite underwent the deployment of its solar arrays in the initial orbit. Subsequently, the on-orbit performance of various subsystems, including the electrical power subsystem, communication subsystem, on-board data handling subsystem, thermal control subsystem, and attitude and orbit control subsystem, were validated. The validation results demonstrate that the platform's function and performance adequately support the payloads for on-orbit verification and long-term operation. Notably, the performance of the attitude control subsystem exceeds the design expectations. The

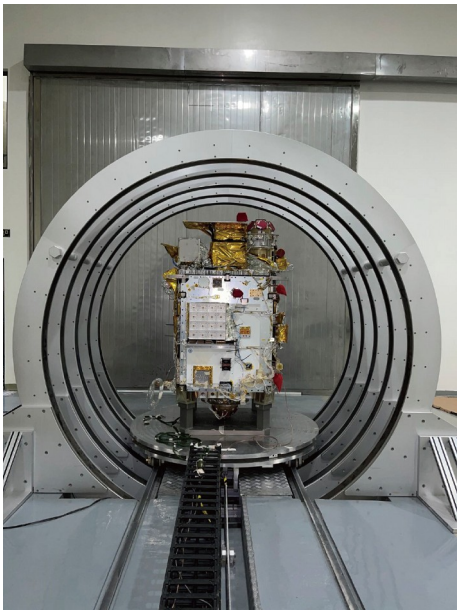

Figure 29 Magnetic test of SATech-01.

inertial attitude control precision achieved is better than 0.005° (3σ), surpassing the design value of 0.1° (as depicted in Figure 30). Furthermore, the attitude control stability is better than 0.0005°/s (3σ), outperforming the design value of 0.003° (as shown in Figure 31).

6.2 HEBS

The commissioning observation of HEBS starts on August 4th, 2022. Since then, HEBS has been routinely detecting gamma-ray transients (gamma-ray bursts, soft gamma-ray repeater, solar flares, etc.) and sending near real-time trigger alerts.

During the commissioning phase, the in-flight background of GRD and the in-flight performance of SiPM were analysed. The performance of HEBS has been intensively optimized after the calibration, which uses in-flight energy lines to derive the in-flight energy gain calibration and detector response matrix. Besides, two relatively bright GRBs and some gamma-ray repeaters (SGRs) with joint observations are used for the cross-calibration work of the HEBS GRD detectors, respectively. There is a very good agreement between HEBS GRDs and the other well-calibrated instruments (i.e., Fermi/GBM and Swift/BAT). Meanwhile, there is also good agreement between GRD detectors of HEBS. Those optimizations pave the way for HEBS to accurately observe the exceptional bright GRB 221009A.

GRB 221009A is the brightest gamma-ray burst ever detected since the discovery of this kind of energetic explosion. However, an accurate measurement of the prompt emission properties of this burst is very challenging due to its exceptional brightness. With joint observations of Insight-HXMT and HEBS, we made an unprecedentedly accurate measurement of the emission during the first ~1800 s of GRB 221009A, including its precursor, main emission (ME, which dominates the burst in flux), flaring emission and early afterglow, in the hard X-ray to the soft gamma-ray band from ~10 keV to ~6 MeV. Figure 32 shows the light curve of GRB 221009A measured by HEBS/GRD01, and more data and analysis are available in ref. [11]. Based on the HEBS unsaturated data of the ME, we measure a record-breaking isotropic equivalent energy ($E_{\rm iso}$) of ~1.5×10^{55} erg, which is about eight times the total rest-mass energy of the Sun.

6.3 LEIA

During the performance verification phase in August and September 2022, LEIA conducted a series of test observations spanning several days. The observations targeted specific sky regions and objects, including the Galactic center, the Magellanic Clouds, Sco X-1, Cas A, Cyg Loop, and several extragalactic sources.

The observations were performed in Earth's shadow to eliminate the effects of the Sun, starting 2 min after the satellite entering the shadow and ending 10 min before leaving it, resulting in an observational duration of ~23 min in each orbit. The CMOS detectors were operating in the event mode.

The initial results from the first in-flight experiments of LEIA show that the levels of the diffuse X-ray sky background, which dominates the energy band <2 keV, agree generally with the simulation. The particle background during the usable observational duration is ~10 cts s^{-1} per

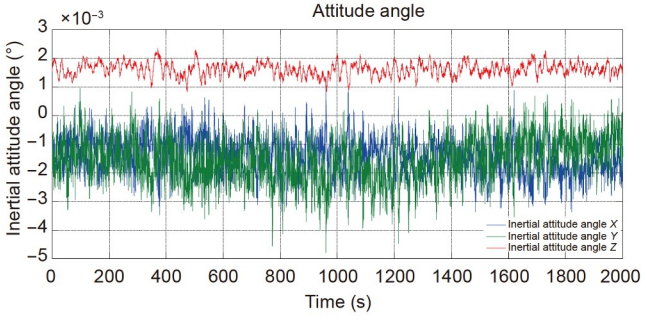

Figure 30 Attitude angle deviation in inertial coordinates.

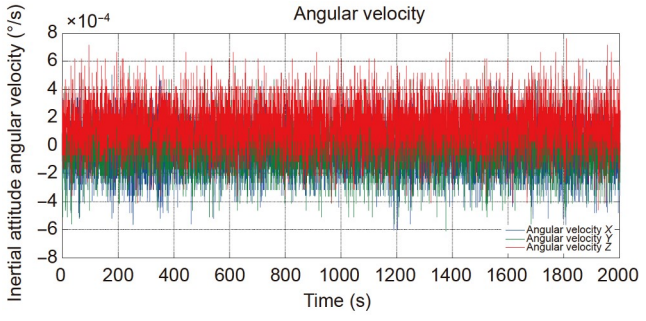

Figure 31 Attitude angle velocity in inertial coordinates.

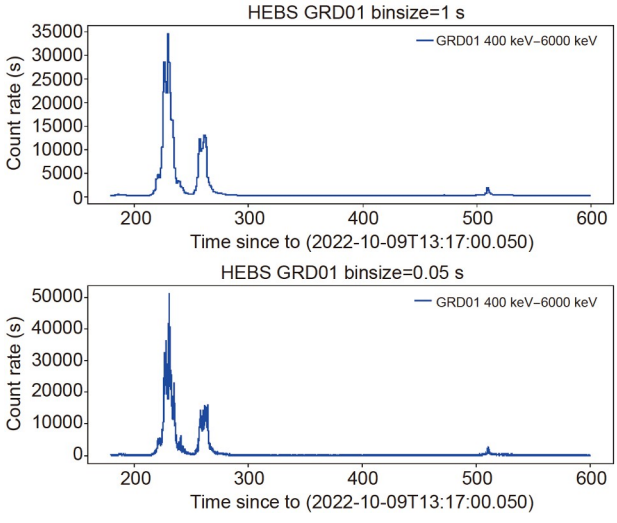

Figure 32 HEBS/GRD01 light curve of GRB 221009A.

CMOS in 0.5–4 keV, which is twice the simulated value. Figure 33 (left) shows the X-ray image of the Galactic centerregion (centering on l=6.6°, b=0.9°), observed in one pointing with a net exposure of 798 s on August 10th, 2022. Within the FoV of 18.6°×18.6°, 14 sources are detected at significance levels ≥5σ in one snapshot. This is the first widefield X-ray image of celestial bodies ever taken by a focusing imaging telescope [2].

This has remarkable implications for both the technology and science of soft X-ray sky monitoring. Initial results from the LEIA experiment, which are the first truly widefield X-ray images of celestial bodies ever taken by a focusing imaging X-ray telescope with oneshot exposures.

6.4 SUTRI

The aperture door of SUTRI was opened on August 31st, 2022. SUTRI's observing plans are the combination of four modes, i.e., the routine observing mode, the dark calibration mode, the flat field calibration mode, and the cleaning mode. The routine observing mode is the master mode. The cleaning mode is designed in the thermal control system. Once there is obvious degradation from the CMOS sensor, the SUTRI will work in cleaning mode for a period of time. The dark calibration and the flat field calibration modes calibrate the dark current and the instrumental pixel-to-pixel nonuniformity.

Since September 4th, 2022, SUTRI has been routinely taking narrow-band images of the solar upper transition region during the roughly two-thirds of each orbit period (~60/96 min). SUTRI has observed many solar flares, coronal mass ejections (CMEs), prominences/filaments, and their eruptions so far, demonstrating SUTRI's capability to monitor solar eruptions. The network structures of transition region, active region loops, jets, and coronal holes are also seen in the images taken by SUTRI. With a formation temperature of ~0.5 MK, the Ne VII 46.5 nm line is an excellent one for the diagnostics of cooling downflows in the upper solar atmosphere. The newly developed Sc/Si multi-layer reflecting mirror and the CMOS camera are validated on-orbit. Routine calibration data is also taken to monitor the long-term behavior of SUTRI.

SUTRI data are categorized into different levels: Level 0, Level 0.9, Level 1, and Level 1.5. Figure 34 illustrates the data processing workflow from Level 0 to Level 0.9 [4]. At the Huairou Solar Observing Station (HSOS) of the National Astronomical Observatories of China (NAOC), the data server utilizes a data processing pipeline to generate high-level calibration and scientific data. The quick-look and high-level science data produced by the pipeline are stored in the SUTRI archive. These data are made publicly available free of charge and can be downloaded from the SUTRI website starting on January 11th, 2023 (https://sun10.bao.ac.cn/SUTRI/). Despite being a low-cost experiment, SUTRI's observations are expected to significantly contribute to our understanding of mass and energy transport processes in the solar atmosphere.

6.5 CPT

On November 7th, 2022, after the non-magnetic telescopic mast (TM) was deployed, the payload entered the long-term on-orbit working phase, achieving the first global magnetic field measurement using a NSSC developed quantum/atomic magnetometer. The on-orbit optimization test of the payload was completed on December 5th, 2022. In the following 10 days, the satellite flew 152 orbits around the Earth (Orbit No. 1991–2143), and the global geomagnetic total field measurement is shown in Figure 35. During satellite attitude adjustment, data is missing, as shown in Figure 35(a), since the CPTM lost tracking to the field, due to interference from the magnetic torque of the satellite and vibration of the

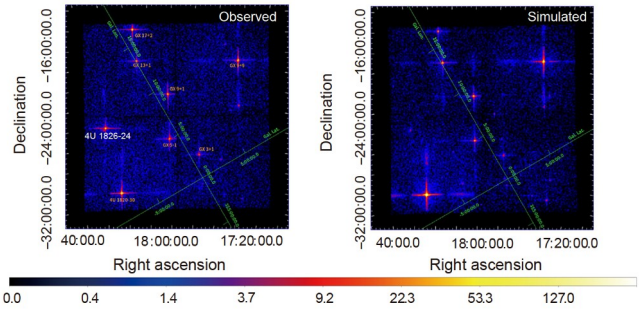

Figure 33 First-light X-ray image of the Galactic center region obtained by LEIA in a one-shot observation of 798 s in 0.5–4 keV, covering a field of view of 18.6°×18.6° (left). The simulated observation of the same patch of sky is also shown for comparison (right). The observation identifies a source (4U 1826-24) that had become obviously much brighter than viewed at a previous observation. Colors represent counts per pixel.

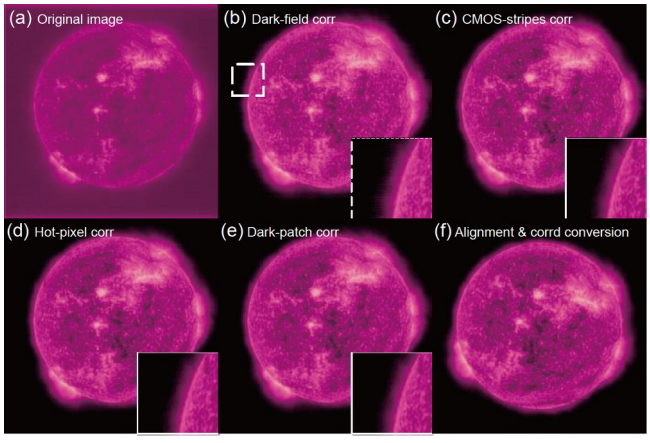

Figure 34 An example of SUTRI's data processing from Level 0 to Level 0.9. To better illustrate the improvement of the scientific data in each step, the sub-images at the right and bottom corner of (b)–(e) show the zoom-in images of the white box region marked in (b).

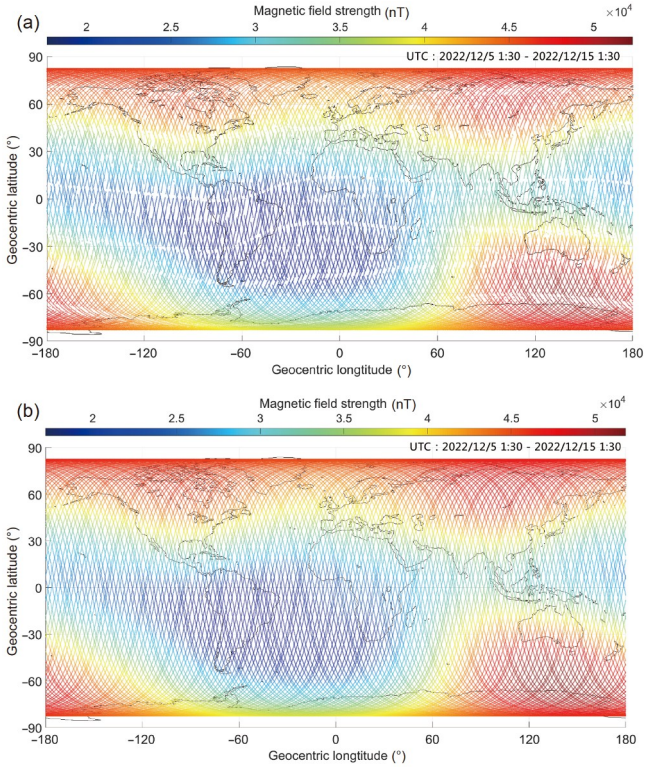

Figure 35 Global geomagnetic total field measured by the CPT magnetometer and AMR magnetometer.

sensor bench on the TM, and re-tracked automatically afterward. In Figure 35(b), the total field was calculated from AMRM three axis vector data without calibration by the CPTM. The NST has successfully provided the precise attitude of the sensor bench on-orbit, and obtained the rotation angle of the sensor bench relative to the satellite. In the shadow, the NST is stable to the satellite with a standard deviation of 30″ (1σ), and average Euler angles from the NST to the satellite is [−89.49°, 0.08°, 90.11°] in "*X*-*Y*-*Z*" rotation sequence, as shown in Figure 36. On the boundaries of shadow, the maximum angle fluctuation relative to the satellite is about ±2° due to the vibration of the satellite during the attitude adjustment and the thermal deformation of the TM.

The magnetometers have entered the normal operating phase. On-orbit calibration, on-orbit data analysis, comparison with other satellite data, comparison with geomagnetic model data, and scientific research will be carried out further.

6.6 Other payloads

In addition to the scientific payloads, other payloads have also successfully completed their respective verification processes during the first phase.

The space curing verification platform for inorganic materials was specifically designed to assess the curing performance of fiber-reinforced inorganic composites that can be folded on the ground and then permanently extended and cured in the microgravity environment of space. During the on-orbit test, the inorganic composites were heated, and images of the material surface were captured to evaluate the internal curing condition of the fiber-reinforced inorganic composites. The results of the test indicated that the effective heating duration met the expected value, and the cured inorganic material exhibited the desired characteristics (Figure 37). No structural damage was observed, and the material was successfully cured in orbit. These findings provide valuable insights and technical groundwork for the future development of large inflatable unfolded flexible space capsules.

Three remote-sensing cameras have successfully achieved optimal performance following their commissioning. Figure 38 showcases the on-orbit images captured by the all-alu-

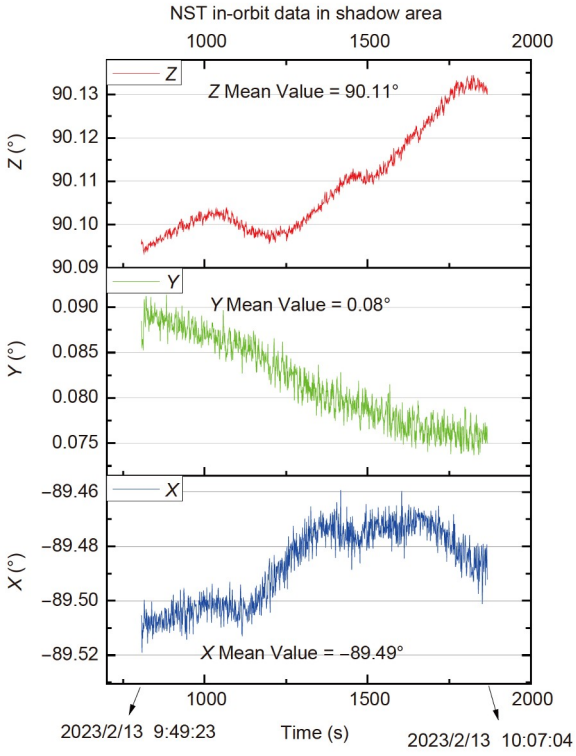

Figure 36 Euler angles from the NST to satellite according to a *XYZ* rotation.

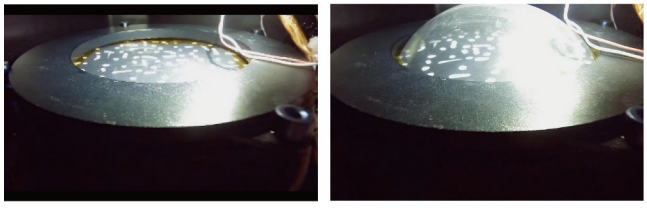

Figure 37 Image information of inorganic material cured and tested on-orbit (left: Pre-test; right: Post-test).

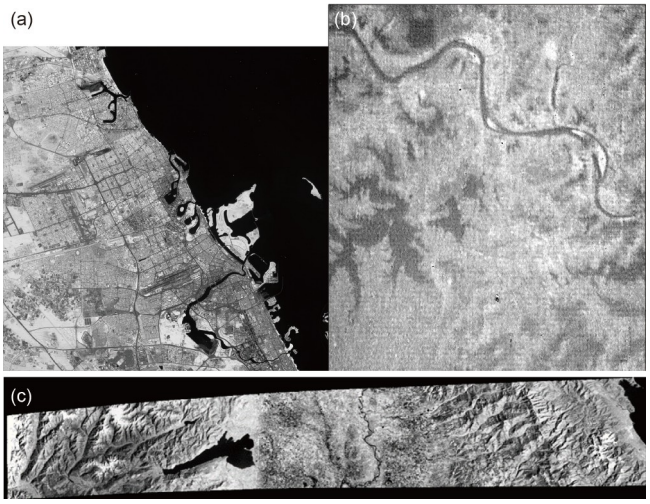

Figure 38 (a) Image taken by all-aluminum freeform imaging telescope; (b) image taken by parasitic infrared camera with cryogenic optics; (c) image taken by multi-functional integrated imager.

minum freeform imaging telescope, parasitic infrared camera with cryogenic optics, and multi-functional integrated imager, respectively.

7 Conclusion

This paper provides an overview of SATech-01, encompassing its technical description, on-orbit performance, and scientific payload since its launch. SATech-01 has successfully completed the first stage, which involved verification, calibration, and commissioning. During this phase, the satellite's operations, functions, and performance largely met the specified requirements. Going forward, the satellite will undergo long-term verification, routine observation, and joint observation of targets of opportunity.

This work was supported by the Strategic Priority Program on Space Science, the Chinese Academy of Sciences.

1 Zhang D, Zheng C, Liu J, et al. The performance of SiPM-based gamma-ray detector (GRD) of GECAM-C. Nucl Instrum Meth Phys Res Sect A, 2023, 1056: 168586
2 Zhang C, Ling Z X, Sun X J, et al. First wide field-of-view X-ray observations by a lobster-eye focusing telescope in orbit. Astrophys J Lett, 2022, 941: L2
3 Ling Z X, Sun X J, Zhang C, et al. The lobster eye imager for astronomy onboard the SATech-01 satellite. Res Astron Astrophys, 2023, 23: 095007
4 Bai X, Tian H, Deng Y, et al. The solar upper transition region imager (SUTRI) onboard the SATech-01 satellite. Res Astron Astrophys, 2023, 23: 065014
5 Lu S, Luo W, Long J, et al. Numerical simulation optimization of neutral flow dynamics in low-power Hall thruster. Results Phys, 2023, 46: 106268
6 Gao R, Li J, Wang P, et al. The opto-mechanical-thermal coupling analysis and verification of an all-aluminum freeform imaging telescope. Symmetry, 2022, 14: 2391
7 Huang C, Li J, Cai Z, et al. Post optical freeform compensation technique for machining errors of large-aperture primary mirror. Photonics, 2023, 10: 768
8 Mai Z, Zhu X, Li H, et al. Experiment study of single event functional interrupt in analog-to-digital converters using a pulsed laser. Electronics, 2023, 12: 2774
9 Xin J, Zhu X, Ma Y, et al. Study of single event latch-up hardness for CMOS devices with a resistor in front of DC-DC converter. Electronics, 2023, 12: 550
10 Liu L, Zhang X F, Liang H, et al. Deployable and self adaptive system of intelligent thermal control of a micro satellite. In: Proceedings of the 2022 International Conference on Sensing, Measurement & Data Analytics in the Era of Artificial Intelligence (ICSMD). Harbin, 2022. 1–6
11 GRB 221009A: HEBS detection, GCN Circular 32751, 2022. Available from https://gcn.nasa.gov/circulars/32751?query=221009A